Supporting Information

for

An Inversion Layer at the Surface of *n*-type Iron Pyrite

Moritz Limpinsel,[1] Nima Farhi,[2] Nicholas Berry,[3] Jeffrey Lindemuth,[4] Craig L. Perkins,[5] Qiyin Lin,[6] Matt Law[1,2,6]

[1]Department of Chemistry, University of California, Irvine, Irvine, CA 92697
[2]Dept. of Chemical Engineering and Materials Science, University of California, Irvine, Irvine, CA 92697
[3]Department of Physics and Astronomy, University of California, Irvine, Irvine, CA 92697
[4]Lake Shore Cyrotronics, Inc., 575 McCorkle Blvd, Westerville, OH 43082
[5]National Renewable Energy Laboratory, Golden, CO
[6]Laboratory for Electron and X-ray Instrumentation, University of California, Irvine, Irvine, CA 92697
email: matt.law@uci.edu

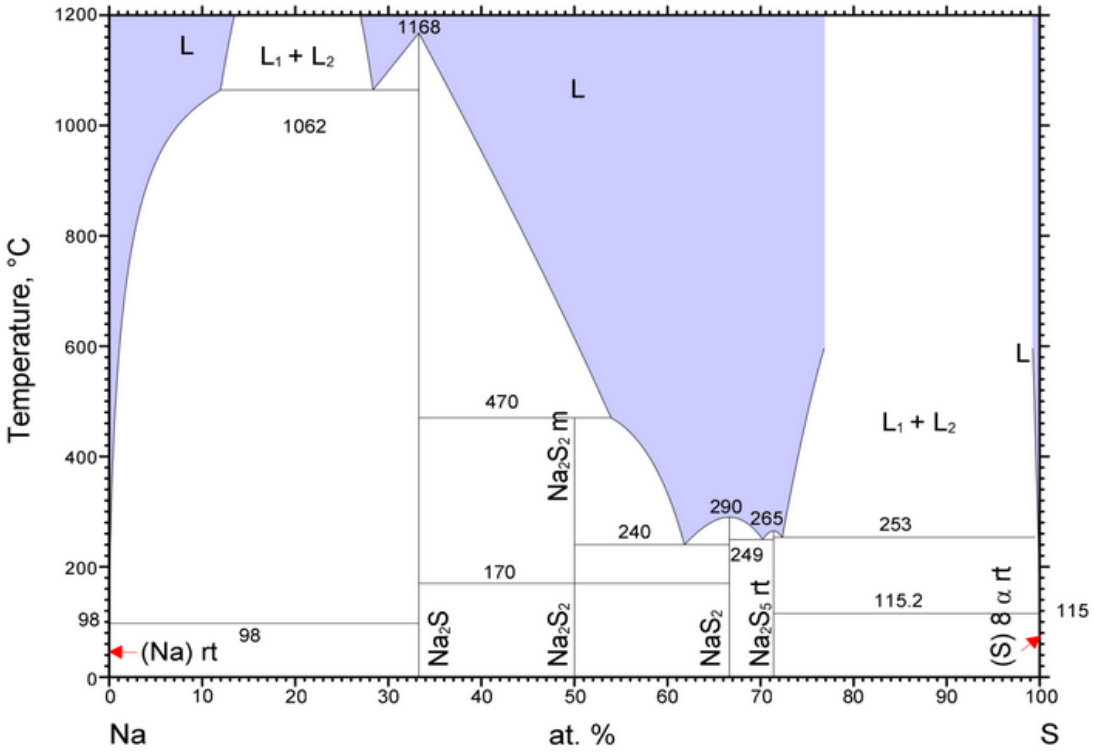

Figure S1. The Na-S binary phase diagram (data from J. Sangster and A. D. Pelton, *J. Phase Equilib*., 1997, **18**, 89.). Mixtures of Na_2S and S have eutectics as low as 240°C. There is also a region of binary liquid immiscibility above 253°C near the sulfur-rich end of the system.

Single Crystal Structural Determination

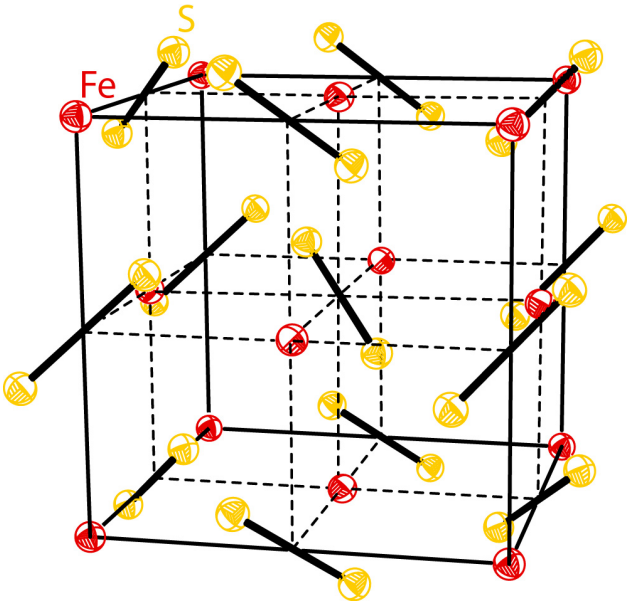

Figure S2. A view of the experimentally-determined pyrite unit cell with 95% thermal contours shown for all ions. Red ellipsoids are iron ions; yellow ellipsoids are sulfur ions.

Table S1. Refined Atomic Coordinates, Bond Lengths, and Angles.

Coordinates **[in units of fractional lattice constant]**	
Fe: (0,0,0); (0.5,0.5,0); (0,0.5,0.5); (0.5,0,0.5)	
S: (0.38490,0.38490,0.38490); (0.61510,0.61510,0.61510); (0.88490,0.38490,0.11510); (0.11510,0.61510,0.88490); (0.38490,0.11510,0.88490); (0.61510,0.88490,0.11510); (0.11510,0.88490,0.38490); (0.88490,0.11510,0.61510).	
Lengths **[Å]**	
Fe–S	2.2627(2)
S–S	2.1585(7)
Angles **[°]**	
S–Fe–S	94.349(3), 85.651(3)
S–S–Fe	102.345(8)
Fe–S–Fe	115.559(6)

Crystal data and structure refinement.

Empirical formula	FeS_2
Formula weight	119.975
Temperature	143(2) K
Wavelength	0.71073 Å
Crystal system	Cubic
Space group	P a -3

Unit cell dimensions	a = 5.4143(5) Å	α = 90°
	b = 5.4143(5) Å	β = 90°
	c = 5.4143(5) Å	γ = 90°
Volume	158.72(3) Å^3	
Z	4	
Atomic Coordinates	Fe: (0,0,0); (0.5,0.5,0); (0,0.5,0.5); (0.5,0,0.5)	
	S: (0.38490,0.38490,0.38490); (0.61510,0.61510,0.61510); (0.88490,0.38490,0.11510); (0.11510,0.61510,0.88490); (0.38490,0.11510,0.88490); (0.61510,0.88490,0.11510); (0.11510,0.88490,0.38490); (0.88490,0.11510,0.61510).	
Density (calculated)	5.021 Mg/m^3	
Absorption coefficient	11.477 mm^{-1}	
F(000)	232	
Crystal size	0.33 x 0.25 x 0.11 mm^3	
Crystal color and habit	gold cuboid	
Diffractometer	Bruker Apex II	
Theta range for data collection	11.36 to 42.51°.	
Index ranges	$-10 \le h \le 8$, $-10 \le k \le 10$, $-10 \le l \le 10$	
Reflections collected	4228	
Independent reflections	190 [R(int) = 0.0373]	
Observed reflections (I > 2σ(I))	189	
Completeness to theta = 42.51°	96.9 %	
Max. and min. transmission	0.4443 and 0.2429	
Solution method	SHELXS-97 (Sheldrick, 2008)	
Refinement method	SHELXL-97 (Sheldrick, 2008)	
Data / restraints / parameters	190 / 0 / 9	
Goodness-of-fit on F^2	1.218	
Final R indices [I>2σ(I)]	R1 = 0.0159, wR2 = 0.0398	
R indices (all data)	R1 = 0.0160, wR2 = 0.0399	
Extinction coefficient	1.02(10)	
Largest diff. peak and hole	0.655 and -0.667 e.Å^{-3}	

Table S2. Site Occupancy Factors (SOFs) for Fe and S in Pyrite.

	Fe SOF		ESD	S SOF		ESD
crystal 1	1.00	±	0.07	1.00	±	0.06
crystal 2	0.99	±	0.05	1.00	±	0.05
crystal 3	0.99	±	0.05	0.98	±	0.04
crystal 4	1.01	±	0.03	1.01	±	0.03
crystal 5	1.00	±	0.04	1.00	±	0.05

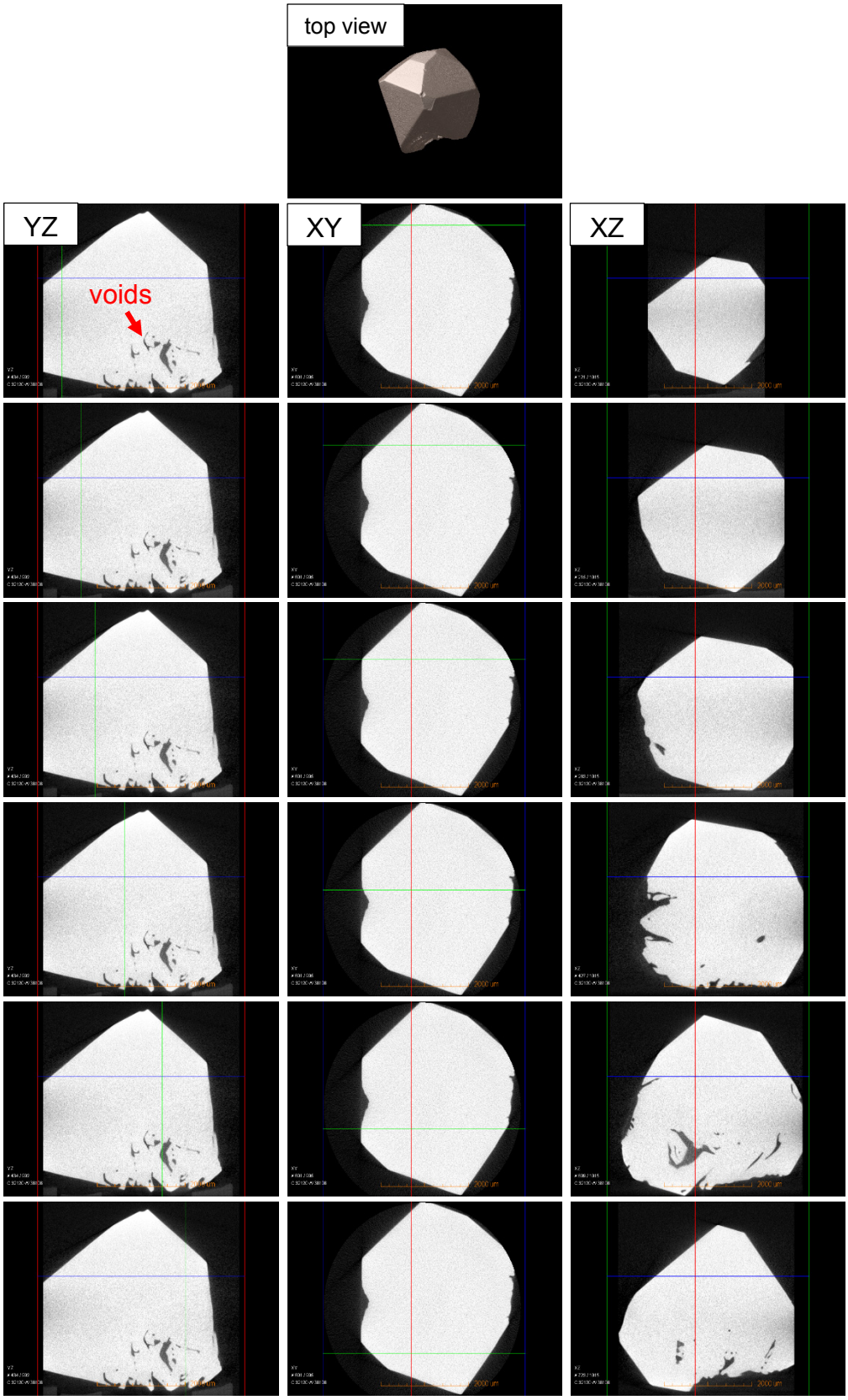

Figure S3. X-ray tomography images of a flux-grown pyrite crystal. (*top*) Top view of a 3D reconstruction

of the crystal. (*left column*) Images of a *yz* cut through the crystal. The horizontal blue line denotes the position of the *xy* cut shown in the middle column. The vertical green lines denote the positions of the *xz* cuts shown in the right column. Voids are present in the bottom half of this crystal. (*middle column*) Images of an *xy* cut through the crystal. The vertical red line denotes the position of the yz cuts shown in the left column. The horizontal green lines denote the positions of the *xz* cuts shown in the right column. (*right column*) Images of a series of *xz* cuts through the crystal, showing voids only in the lower half of the specimen. The scale bar is 2 mm. See Movie S1 for a rotating 3D reconstruction of this crystal.

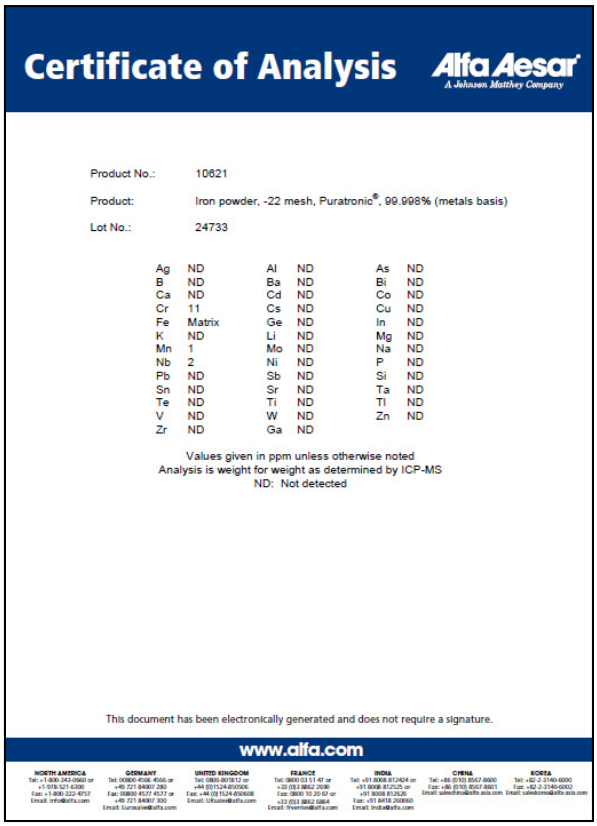

Certificate of Analysis

Alfa Aesar
A Johnson Matthey Company

Product No.: 10621

Product: Iron powder, -22 mesh, Puratronic®, 99.998% (metals basis)

Lot No.: 24733

Ag	ND	Al	ND	As	ND
B	ND	Ba	ND	Bi	ND
Ca	ND	Cd	ND	Co	ND
Cr	11	Cs	ND	Cu	ND
Fe	Matrix	Ge	ND	In	ND
K	ND	Li	ND	Mg	ND
Mn	1	Mo	ND	Na	ND
Nb	2	Ni	ND	P	ND
Pb	ND	Sb	ND	Si	ND
Sn	ND	Sr	ND	Ta	ND
Te	ND	Ti	ND	Tl	ND
V	ND	W	ND	Zn	ND
Zr	ND	Ga	ND		

Values given in ppm unless otherwise noted
Analysis is weight for weight as determined by ICP-MS
ND: Not detected

This document has been electronically generated and does not require a signature.

www.alfa.com

NORTH AMERICA
Tel: +1 800 343 0660 or +1 978 521 6300
Fax: +1 800 322 4757
Email: info@alfa.com

GERMANY
Tel: 00800 4566 4566 or +49 721 84007 280
Fax: 00800 4577 4577 or +49 721 84007 300
Email: kundenkontakt@alfa.com

UNITED KINGDOM
Tel: 0800 801812 or +44 (0)1524 850506
Fax: +44 (0)1524 850608
Email: UKsales@alfa.com

FRANCE
Tel: 0800 03 51 47 or +33 (0)3 8862 2690
Fax: 0800 10 20 67 or +33 (0)3 8862 6864
Email: Frventes@alfa.com

INDIA
Tel: +91 8008 812424 or +91 8008 812525 or +91 8008 812626
Fax: +91 8418 260060
Email: India@alfa.com

CHINA
Tel: +86 (0)10 8567 8600
Fax: +86 (0)10 8567 8601
Email: salesinfo@alfa-asia.com

KOREA
Tel: +82 2 2140 6000
Fax: +82 2 2140 6002
Email: saleskorea@alfa-asia.com

Figure S4. Certificate of analysis for a batch of the iron powder used for pyrite flux synthesis.

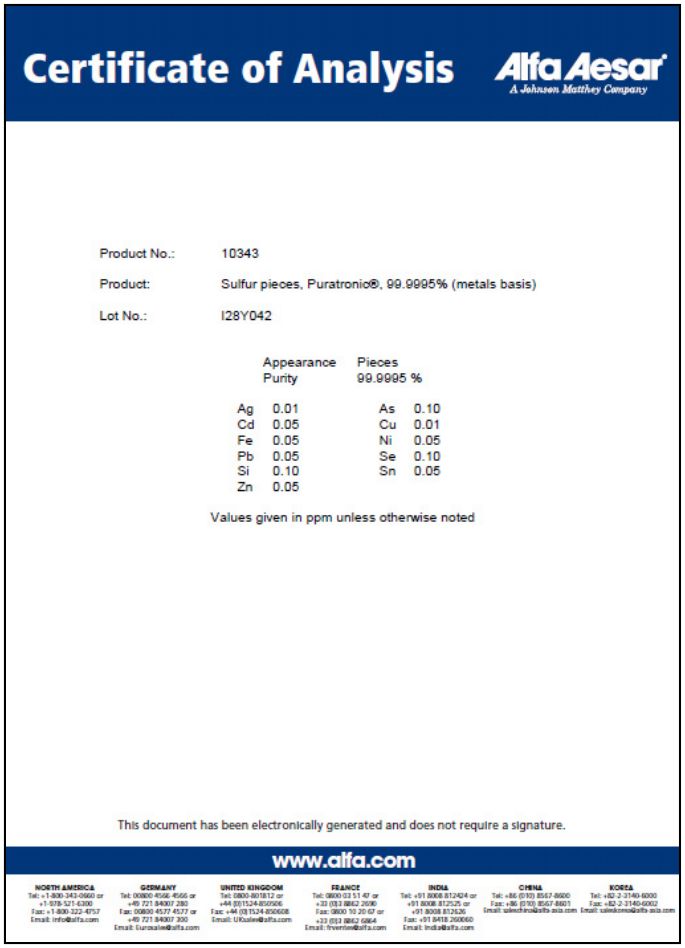

Certificate of Analysis

Alfa Aesar
A Johnson Matthey Company

Product No.: 10343

Product: Sulfur pieces, Puratronic®, 99.9995% (metals basis)

Lot No.: I28Y042

Appearance	Pieces
Purity	99.9995 %

Ag	0.01	As	0.10
Cd	0.05	Cu	0.01
Fe	0.05	Ni	0.05
Pb	0.05	Se	0.10
Si	0.10	Sn	0.05
Zn	0.05		

Values given in ppm unless otherwise noted

This document has been electronically generated and does not require a signature.

www.alfa.com

NORTH AMERICA
Tel: +1-800-343-0660 or +1-978-521-6300
Fax: +1-800-322-4757
Email: info@alfa.com

GERMANY
Tel: 00800 4566 4566 or +49 721 84007 280
Fax: 00800 4577 4577 or +49 721 84007 300
Email: Eurosales@alfa.com

UNITED KINGDOM
Tel: 0800 801812 or +44 (0)1524 850506
Fax: +44 (0)1524 850608
Email: UKsales@alfa.com

FRANCE
Tel: 0800 03 51 47 or +33 (0)3 8862 2690
Fax: 0800 10 20 67 or +33 (0)3 8862 6864
Email: frventes@alfa.com

INDIA
Tel: +91 8008 812424 or +91 8008 812525 or +91 8008 812626
Fax: +91 8418 260060
Email: India@alfa.com

CHINA
Tel: +86 (010) 8567-8600
Fax: +86 (010) 8567-8601
Email: salescnroa@alfa-asia.com

KOREA
Tel: +82-2-2140-6000
Fax: +82-2-2140-6002
Email: saleskorea@alfa-asia.com

Figure S5. Certificate of analysis for a batch of the sulfur powder used for pyrite flux synthesis.

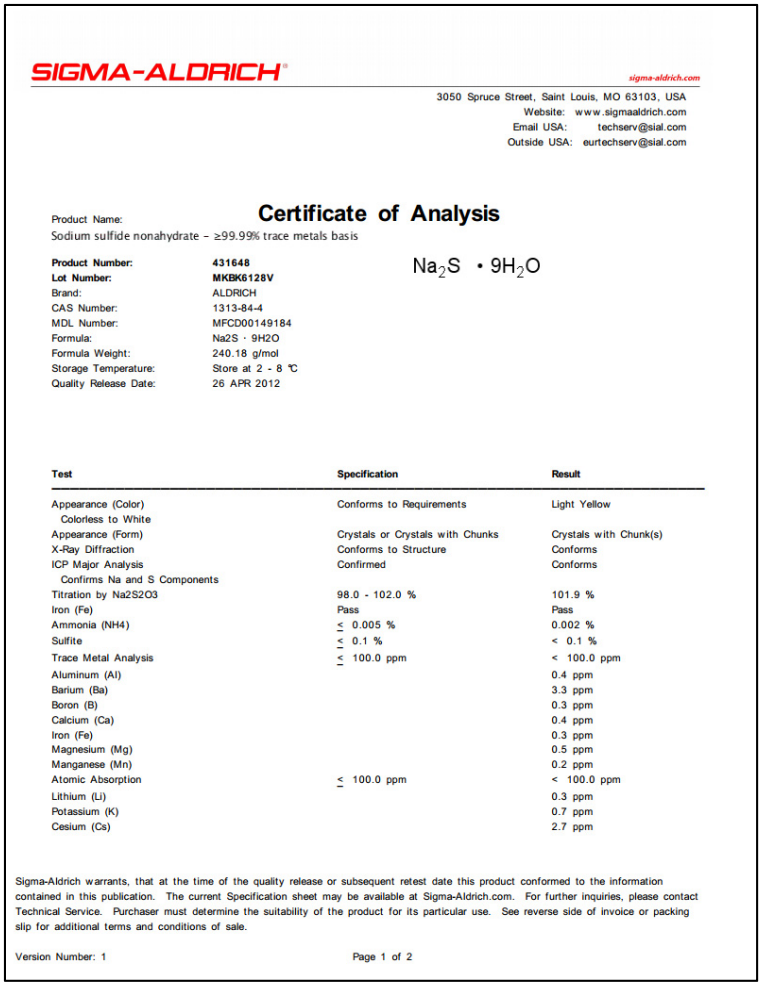

SIGMA-ALDRICH®

sigma-aldrich.com

3050 Spruce Street, Saint Louis, MO 63103, USA
Website: www.sigmaaldrich.com
Email USA: techserv@sial.com
Outside USA: eurtechserv@sial.com

Product Name:
Sodium sulfide nonahydrate - ≥99.99% trace metals basis

Certificate of Analysis

$Na_2S \cdot 9H_2O$

Product Number:	**431648**
Lot Number:	**MKBK6128V**
Brand:	ALDRICH
CAS Number:	1313-84-4
MDL Number:	MFCD00149184
Formula:	Na2S · 9H2O
Formula Weight:	240.18 g/mol
Storage Temperature:	Store at 2 - 8 °C
Quality Release Date:	26 APR 2012

Test	Specification	Result
Appearance (Color) Colorless to White	Conforms to Requirements	Light Yellow
Appearance (Form)	Crystals or Crystals with Chunks	Crystals with Chunk(s)
X-Ray Diffraction	Conforms to Structure	Conforms
ICP Major Analysis Confirms Na and S Components	Confirmed	Conforms
Titration by Na2S2O3	98.0 - 102.0 %	101.9 %
Iron (Fe)	Pass	Pass
Ammonia (NH4)	≤ 0.005 %	0.002 %
Sulfite	≤ 0.1 %	< 0.1 %
Trace Metal Analysis	≤ 100.0 ppm	< 100.0 ppm
Aluminum (Al)		0.4 ppm
Barium (Ba)		3.3 ppm
Boron (B)		0.3 ppm
Calcium (Ca)		0.4 ppm
Iron (Fe)		0.3 ppm
Magnesium (Mg)		0.5 ppm
Manganese (Mn)		0.2 ppm
Atomic Absorption	≤ 100.0 ppm	< 100.0 ppm
Lithium (Li)		0.3 ppm
Potassium (K)		0.7 ppm
Cesium (Cs)		2.7 ppm

Sigma-Aldrich warrants, that at the time of the quality release or subsequent retest date this product conformed to the information contained in this publication. The current Specification sheet may be available at Sigma-Aldrich.com. For further inquiries, please contact Technical Service. Purchaser must determine the suitability of the product for its particular use. See reverse side of invoice or packing slip for additional terms and conditions of sale.

Version Number: 1

Page 1 of 2

Figure S6. Certificate of analysis for a batch of the Na_2S powder used for pyrite flux synthesis.

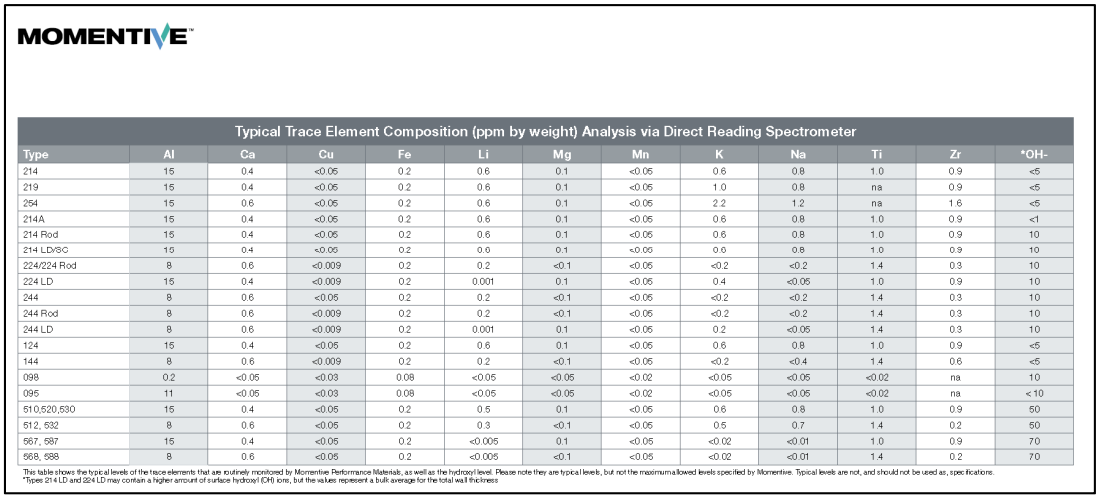

MOMENTIVE™

Typical Trace Element Composition (ppm by weight) Analysis via Direct Reading Spectrometer

Type	Al	Ca	Cu	Fe	Li	Mg	Mn	K	Na	Ti	Zr	*OH-
214	15	0.4	<0.05	0.2	0.6	0.1	<0.05	0.6	0.8	1.0	0.9	<5
219	15	0.4	<0.05	0.2	0.6	0.1	<0.05	1.0	0.8	na	0.9	<5
254	15	0.6	<0.05	0.2	0.6	0.1	<0.05	2.2	1.2	na	1.6	<5
214A	15	0.4	<0.05	0.2	0.6	0.1	<0.05	0.6	0.8	1.0	0.9	<1
214 Rod	15	0.4	<0.05	0.2	0.6	0.1	<0.05	0.6	0.8	1.0	0.9	10
214 LD/SC	15	0.4	<0.05	0.2	0.6	0.1	<0.05	0.6	0.8	1.0	0.9	10
224/224 Rod	8	0.6	<0.009	0.2	0.2	<0.1	<0.05	<0.2	<0.2	1.4	0.3	10
224 LD	15	0.4	<0.009	0.2	0.001	0.1	<0.05	0.4	<0.05	1.0	0.9	10
244	8	0.6	<0.05	0.2	0.2	<0.1	<0.05	<0.2	<0.2	1.4	0.3	10
244 Rod	8	0.6	<0.009	0.2	0.2	<0.1	<0.05	<0.2	<0.2	1.4	0.3	10
244 LD	8	0.6	<0.009	0.2	0.001	0.1	<0.05	0.2	<0.05	1.4	0.3	10
124	15	0.4	<0.05	0.2	0.6	0.1	<0.05	0.6	0.8	1.0	0.9	<5
144	8	0.6	<0.009	0.2	0.2	<0.1	<0.05	<0.2	<0.4	1.4	0.6	<5
098	0.2	<0.05	<0.03	0.08	<0.05	<0.05	<0.02	<0.05	<0.05	<0.02	na	10
095	11	<0.05	<0.03	0.08	<0.05	<0.05	<0.02	<0.05	<0.05	<0.02	na	< 10
510,520,530	15	0.4	<0.05	0.2	0.5	0.1	<0.05	0.6	0.8	1.0	0.9	50
512, 532	8	0.6	<0.05	0.2	0.3	<0.1	<0.05	0.5	0.7	1.4	0.2	50
567, 587	15	0.4	<0.05	0.2	<0.005	0.1	<0.05	<0.02	<0.01	1.0	0.9	70
568, 588	8	0.6	<0.05	0.2	<0.005	<0.1	<0.05	<0.02	<0.01	1.4	0.2	70

This table shows the typical levels of the trace elements that are routinely monitored by Momentive Performance Materials, as well as the hydroxyl level. Please note they are typical levels, but not the maximum allowed levels specified by Momentive. Typical levels are not, and should not be used as, specifications.
*Types 214 LD and 224 LD may contain a higher amount of surface hydroxyl (OH) ions, but the values represent a bulk average for the total wall thickness

Figure S7. Typical trace element composition of the type 214 quartz ampoules used in this study.

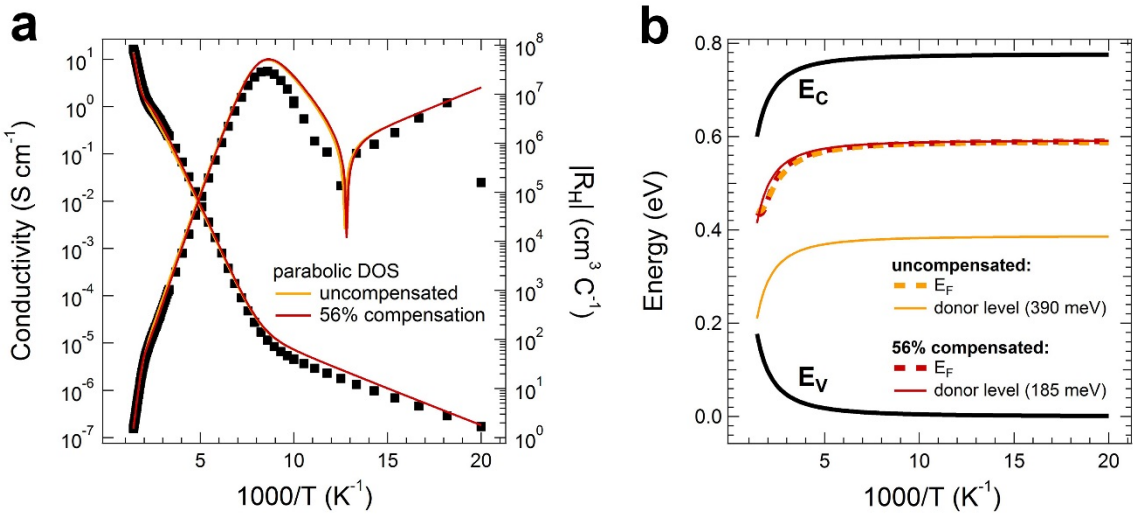

Figure S8. (a) Comparison of fits to the Hall data of Figure 3 assuming zero compensation (yellow traces) and finite compensation (red traces). For the latter, the compensation ratio N_A/N_D was allowed to float freely to achieve a best fit. We found a best fit at 56% compensation with the following bulk parameters: N_D = 1.0×10^{18} cm^{-3}, $E_C - E_D$ = 185 meV, $N_{A,bulk}$ = 5.6×10^{17} cm^{-3}, E_A - E_V = 50 meV. (b) Comparison of E_D and the Fermi level E_F as a function of inverse temperature for the uncompensated case (yellow) and 56% compensated case (red).

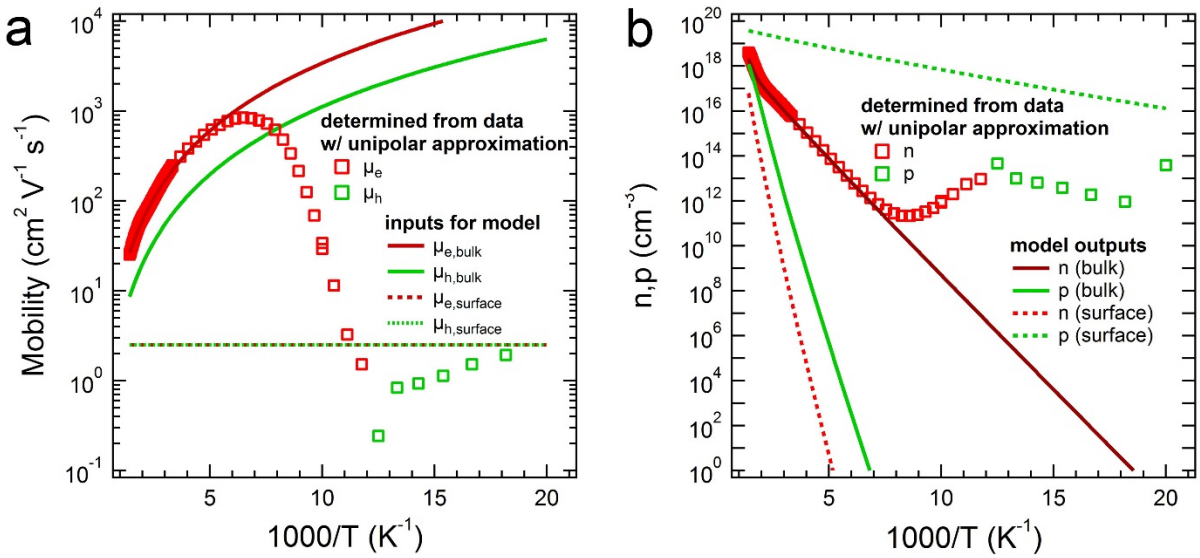

Figure S9. (a) Mobility and (b) concentration of free electrons (red markers) and holes (green markers) as calculated from the Hall data in Figure 3 of the text assuming validity of the unipolar approximation at all temperatures [i.e., $n,p = 1/|R_He|$]. Note that this approximation is violated in regions of mixed electron and hole conduction (i.e., the intrinsic region and the temperature range of 80-150 K). Solid and dashed curves denote the values used to parameterize the model. These values match the data in the unipolar regions (> 150 K for electrons and < 80 K for holes). Electron mobility in the bulk, $\mu_{e,bulk}$, follows a $T^{-2.5}$ dependence at high T, as is common for phonon scattering [C. Jacoboni, C. Canali, G. Ottaviani and A. A. Quaranta, *Sold State Electron*., 1977, **20**, 77]. Hole mobility in the bulk, $\mu_{h,bulk}$, is assumed to be 1/3 of $\mu_{e,bulk}$ at all T. Note that the value of $\mu_{e,bulk}$ is irrelevant at low T and $\mu_{h,bulk}$ is irrelevant at all T due to the low carrier concentrations. Thus, no assumptions about bulk mobility at low T were necessary to model the data. For example, including ionized impurity scattering at low T had no effect on the fits (as expected). Hole mobility in the surface layer, $\mu_{h,surface}$, was estimated from low T data using the unipolar approximation. We found values ranging from 0.1 to 10 cm^2 V^{-1} s^{-1} and used the best fit result of ~2 cm^2 V^{-1} s^{-1} in the model. Electron surface mobility is irrelevant due to negligible carrier concentration and was set to $\mu_{e,surface} = \mu_{h,surface}$ for simplicity. Note that the concentration of holes used to model the surface layer (dotted green line in (b)) is five orders of magnitude higher than the data points because p_{bulk} is calculated from the data is with respect to the bulk while $p_{surface}$ is calculated with respect to just the surface layer, which is about 10^5 times thinner than the bulk.

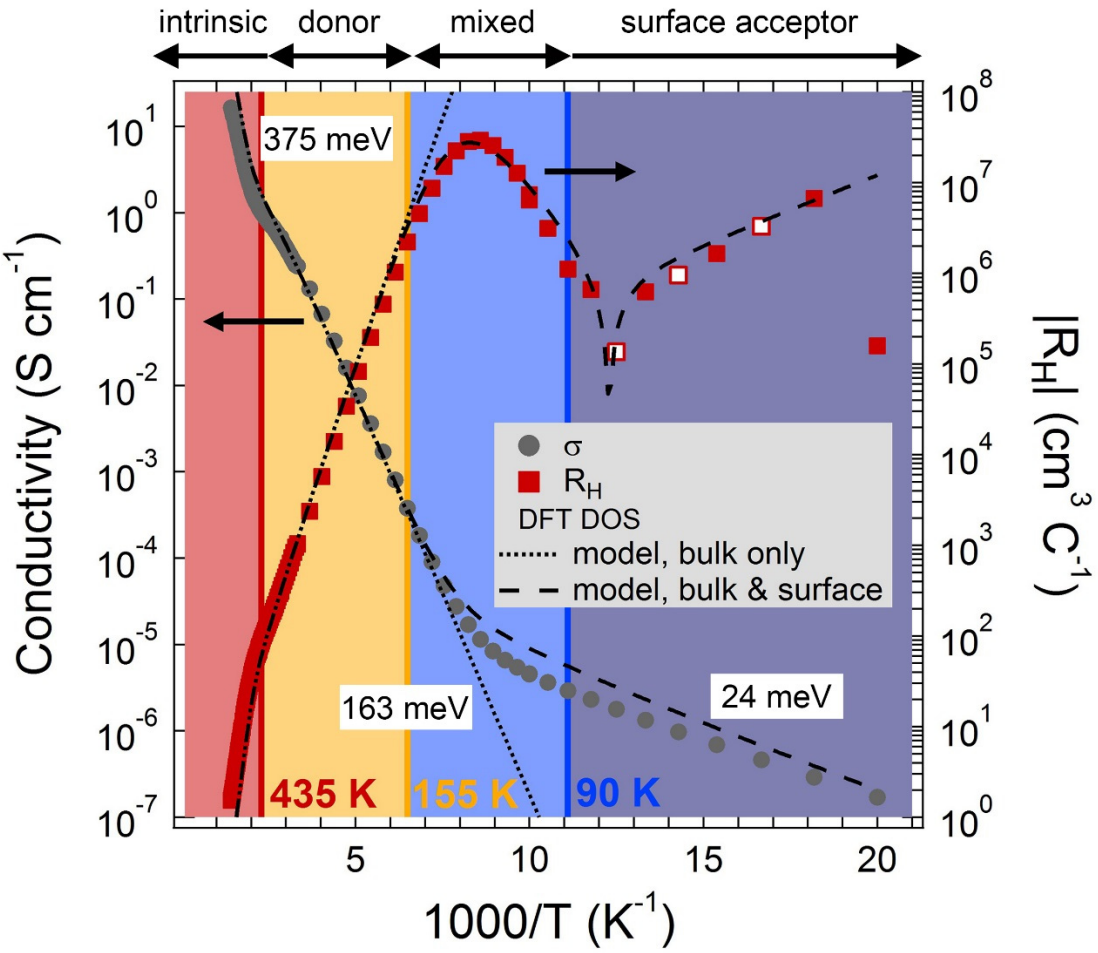

Figure S10. Hall data modeled using the DFT DOS(E) values and the Fermi-Dirac distribution function. Zero compensation is assumed. Parameters used are $N_{D,bulk} = 5.6 \times 10^{19}$ cm^{-3}; $E_C - E_D = 380$ meV; $N_{A,surface} = 4.5 \times 10^{19}$ cm^{-3}; $E_A - E_V = 50$ meV; $d_s = 4.4$ nm; $\mu_h = 2.5$ cm^2 V^{-1} s^{-1}.

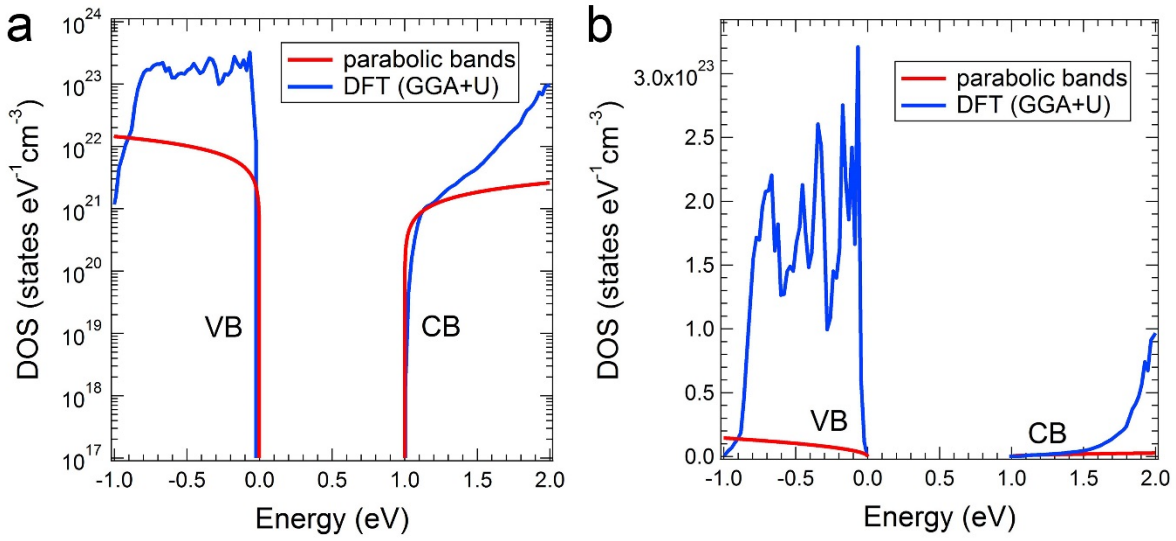

Figure S11. Comparison of DOS(*E*) functions calculated using the normal parabolic band approximation (red) versus density functional theory (GGA+U, blue), on both (a) logarithmic and (b) linear scales. These DOS(*E*) functions were used in the text to model the Hall data and electronic band gap of pyrite. DFT results are taken from J. Hu, Y. Zhang, M. Law and R. Wu, *Phys. Rev. B*, 2012, **85**, 085203.

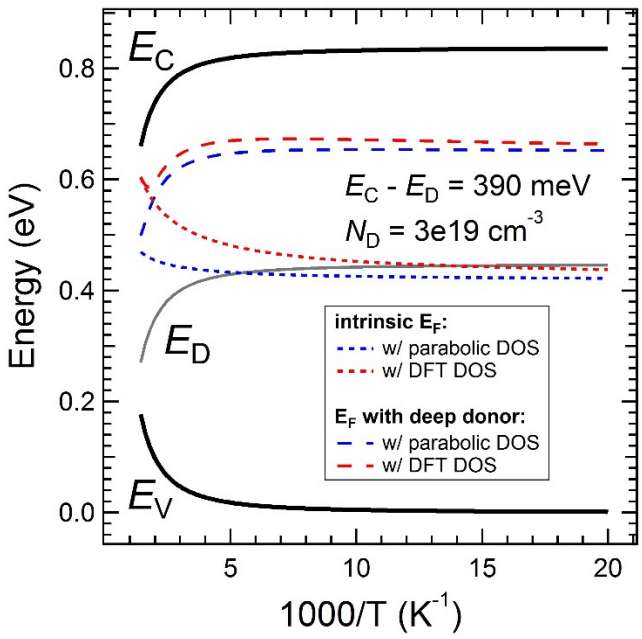

Figure S12. Comparison of the calculated Fermi level as a function of inverse temperature using the parabolic DOS(*E*) versus DFT DOS(*E*) functions. Results are shown for both intrinsic pyrite and pyrite with a deep donor (gray line). Zero compensation is assumed.

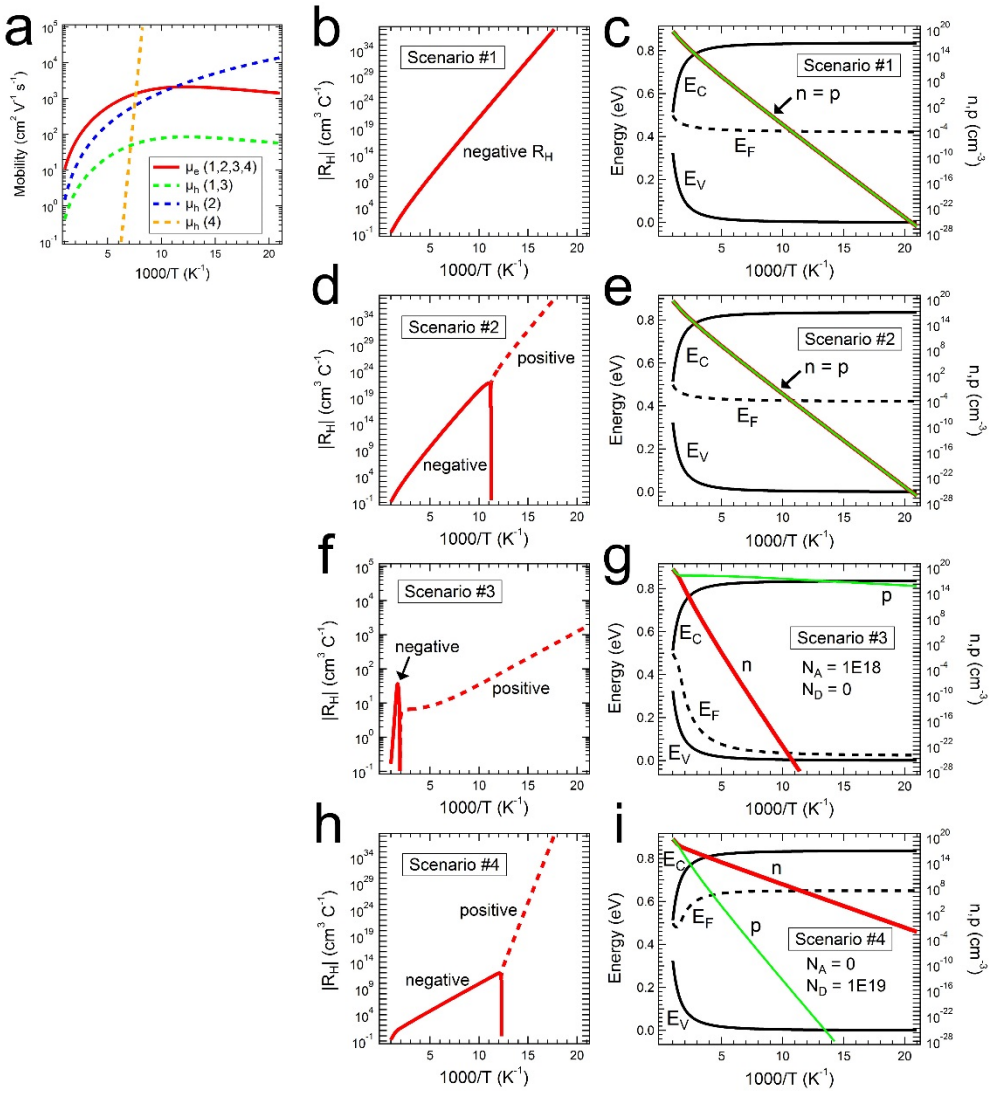

Figure S13. Self-consistent calculations of $|R_H(T)|$ for a homogeneous semiconductor at different combinations of doping and $\mu(T)$. (a) Plots of the mobility functions used to calculate the various scenarios. (b) $|R_H(T)|$ for Scenario #1: intrinsic pyrite with ideal $\mu(T)$ behavior for both electrons and holes and μ_e/μ_h = 25 at all temperatures. R_H is negative at all temperatures because $n = p$ but $\mu_e > \mu_h$. $|R_H|$ increases monotonically as the carriers freeze out. (c) Corresponding band diagram showing E_F (dotted line), n (red line), p (green line), E_V, and E_C versus inverse temperature. (d) $|R_H(T)|$ for Scenario #2: intrinsic pyrite with $\mu_h > \mu_e$ below ~90 K. Since $n = p$, R_H takes the sign of whichever carrier has the higher mobility. Therefore, R_H changes sign at ~90 K. Since the flux crystals are far from intrinsic, this scenario is not relevant to the case at hand. (e) Corresponding band diagram. (f) $|R_H(T)|$ for Scenario #3: $N_D = 0$, $N_A = 10^{18}$ cm^{-3} (E_A - E_V = 50 meV) with ideal $\mu(T)$ behavior for both electrons and holes and $\mu_e/\mu_h = 25$ at all temperatures. R_H is negative in the intrinsic region because $n \approx p$ but $\mu_e > \mu_h$. R_H changes sign when $p > n$ outside of the intrinsic region due to the acceptor doping. This R_H behavior is typical for doped semiconductors. (g) Corresponding band diagram. (h) $|R_H(T)|$ for Scenario #4: $N_D = 10^{19}$ cm^{-3} (E_C - E_D = 390 meV), $N_A = 0$ with $\mu_h >> \mu_e$ below ~90 K due to an exponentially increasing $\mu_h(T)$ with decreasing temperature. This type of non-physical $\mu_h(T)$ function is required in order to overcome the large difference between n and p and force R_H to change sign at low temperatures. The physical irrelevance of this scenario illustrates the practical impossibility of an R_H sign change occurring in a homogeneous doped semiconductor outside of the intrinsic region. (i) Corresponding band diagram. All calculations employed parabolic DOS(E) functions.

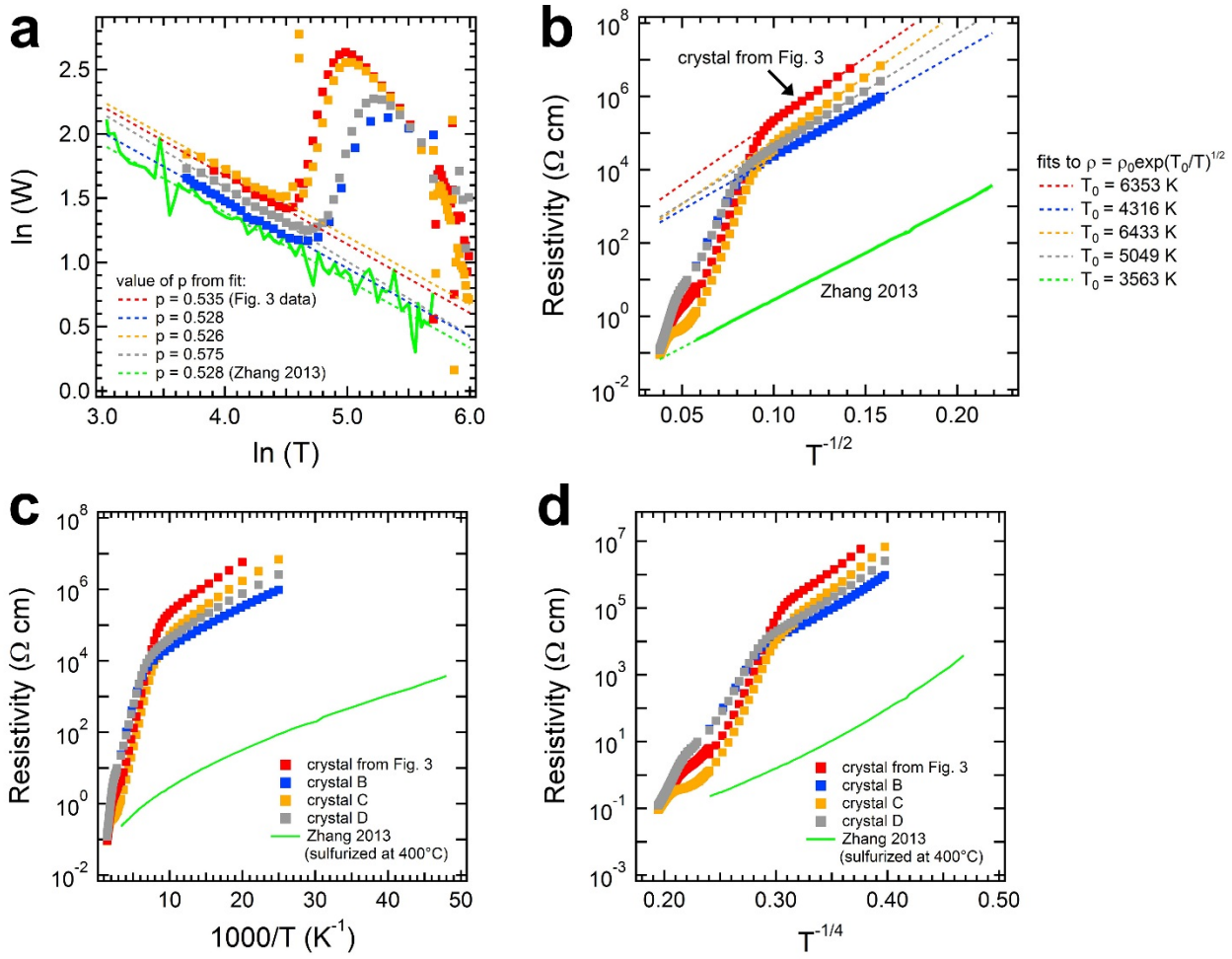

Figure S14. Low-temperature resistivity data and fits. (a) Logarithmic derivative plots to linearize $\rho(T) = \rho_0 \exp[(T_0/T)^p]$ in order to determine the value of p. Here, $\ln(\mathrm{W}) = \ln\left(-\frac{d(\ln \rho)}{d(\ln T)}\right)$. Data are shown for four pyrite single crystals (including the crystal used in Figure 3 of the text), plus a mixed-phase thin film annealed at 400°C from Reference 30 (Zhang 2013). The value of p ranges from 0.53 to 0.58. (b) The data plotted versus $T^{-1/2}$, along with fits to the linear regions at low temperature. The value of T_0 ranges from 3550 to 6350 K. (c) Plots versus T^{-1} and (d) $T^{-1/4}$.

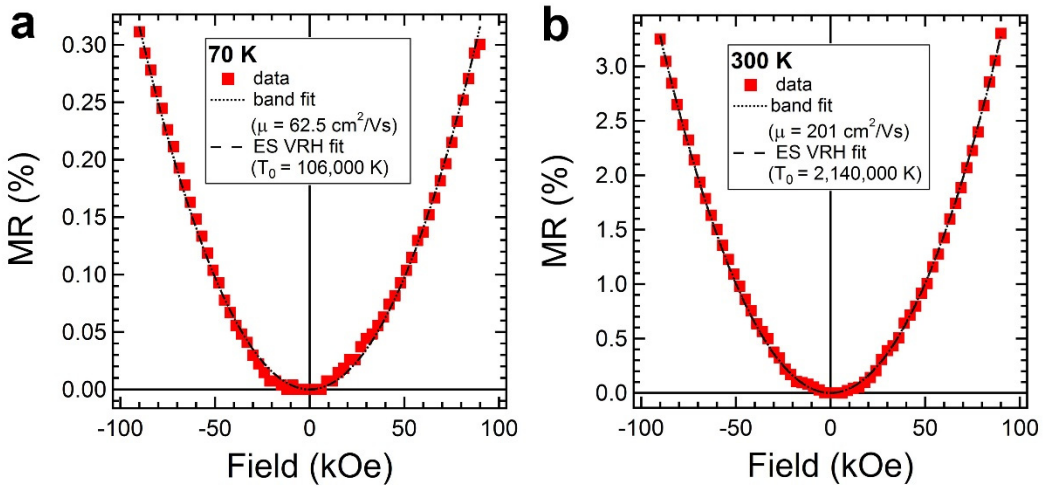

Figure S15. Band transport and ES VRH fits of the MR(H) data for the sample in Figure 4. (a) 70 K data and (b) 300 K data. Qualitatively, the fits are equally good at both temperatures. However, the fits at 70 K result in unphysically large values of μ and T_0, suggesting that the MR is neither simple band nor ES VRH transport. At 300 K, the value of μ is quite reasonable, but that of T_0 is again unphysically large. The ES VRH fits shown here assume a = 6.6 Å.

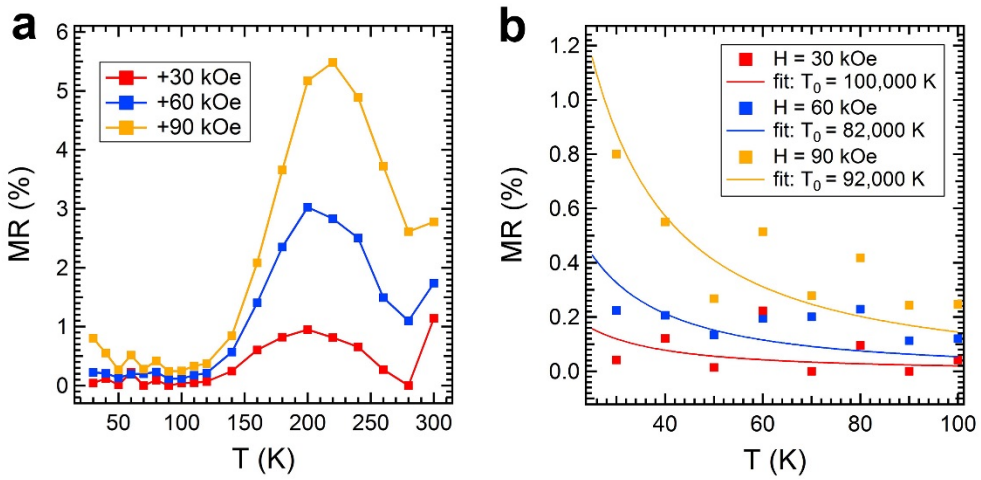

Figure S16. Temperature dependence of the magnetoresistance (MR). (a) Data for a representative sample from 30-300 K at three different values of the magnetic field. (b) Detail view of the low-temperature region, including fits to Eq. 2. While the data at 30 and 60 kOe are too scattered to determine the temperature dependence of the MR, the MR at 90 kOe clearly increases with decreasing temperature in qualitative agreement with Eq. 2. However, an unphysically large value of T_0 is required to fit the data.

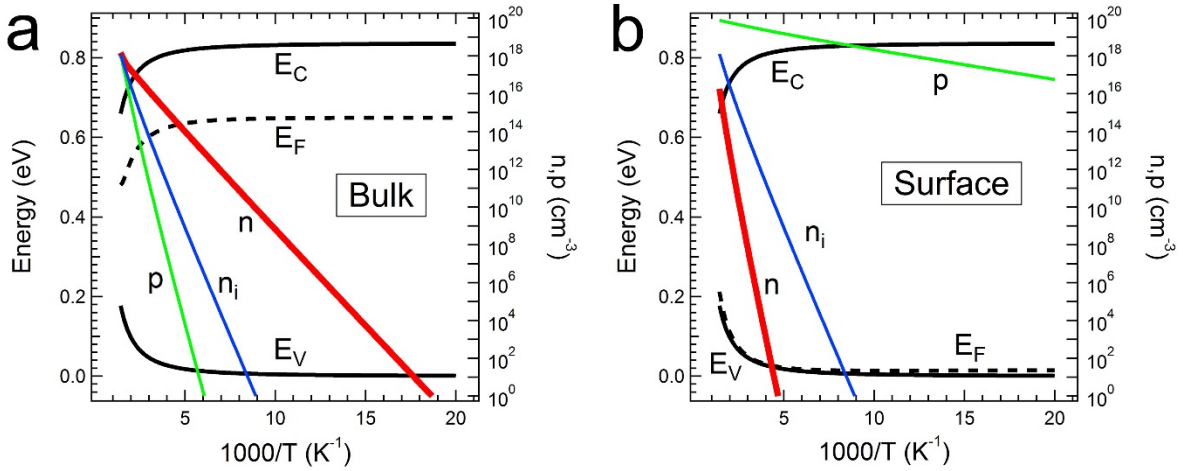

Figure S17. Typical examples of calculated E_F and carrier concentrations as a function of inverse temperature for the (a) bulk and (b) surface layers. Zero compensation is assumed.

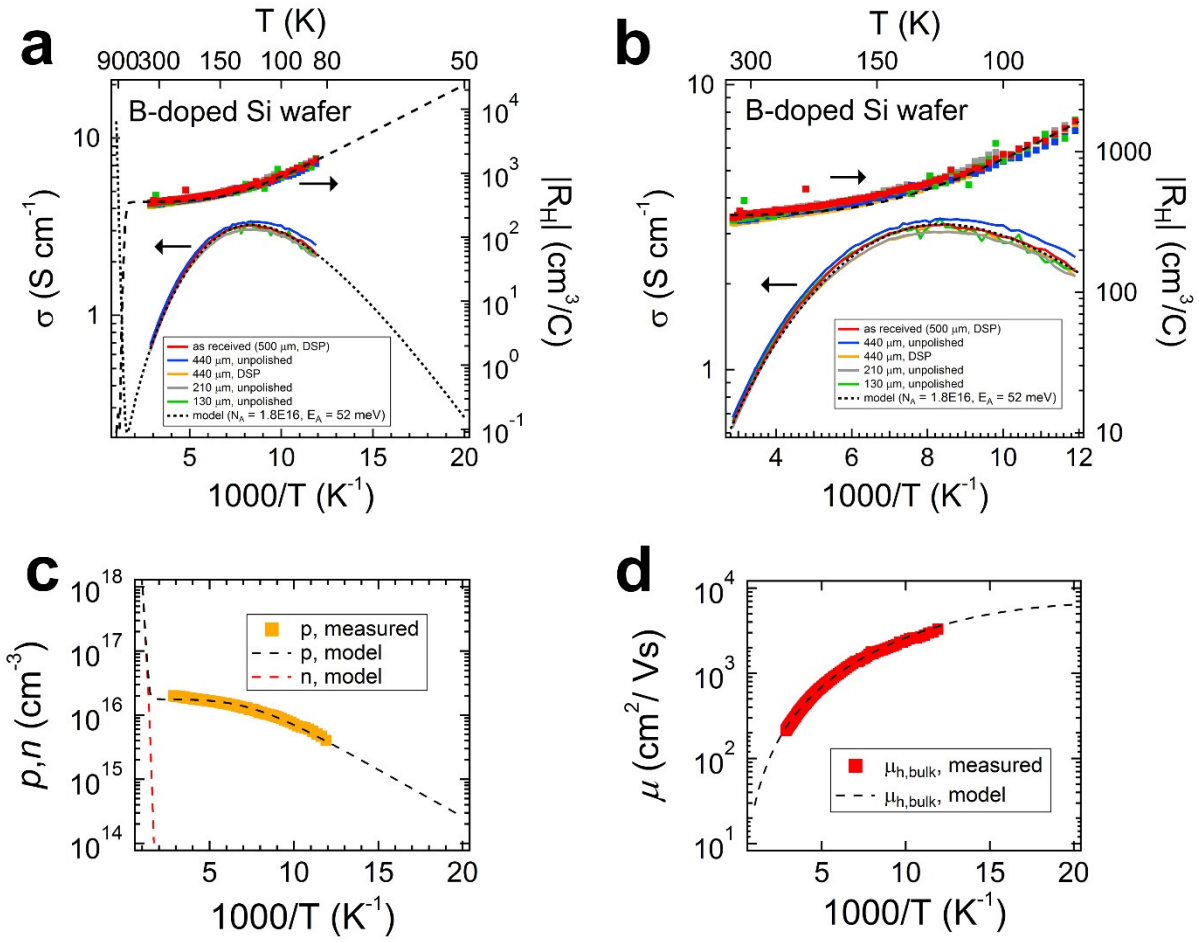

Figure S18. (a) Temperature dependence of the Hall coefficient and conductivity of a boron-doped silicon single crystal as a function of crystal thickness. The data (80-350 K) are independent of thickness and surface polishing, showing that silicon lacks the type of conductive surface layer found on pyrite. The dotted/dashed curves are fits from the model (giving an acceptor concentration of 1.8×10^{16} cm^{-3} and an ionization energy of 52 meV, close to the accepted value of 45 meV for boron in silicon). DSP = double side polished. (b) Magnified view of the temperature range from 80-350 K. (c) Carrier concentration and (d) mobility for the as-received 500 µm thick wafer. These control experiments provide additional confirmation that our model and interpretation of the pyrite data are correct.

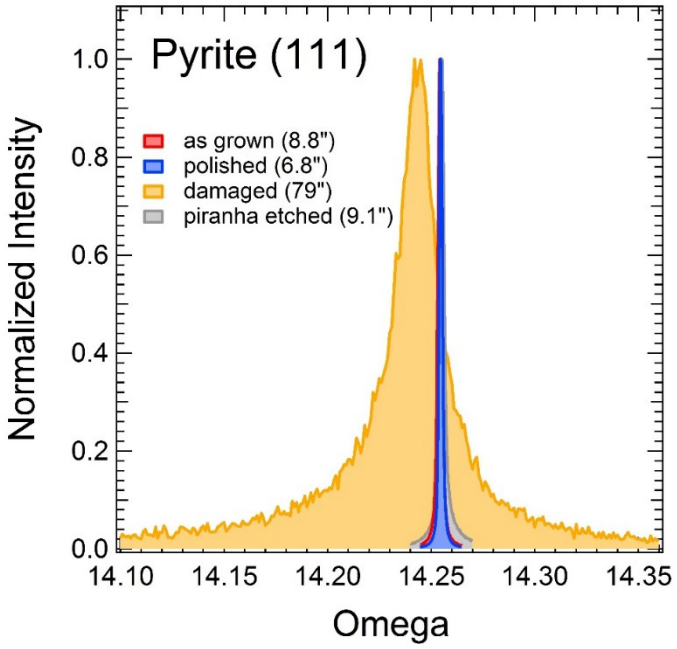

Figure S19. (111) rocking curves for a pyrite slab as a function of surface modification. FWHM values are given in the legend in units of arcseconds.

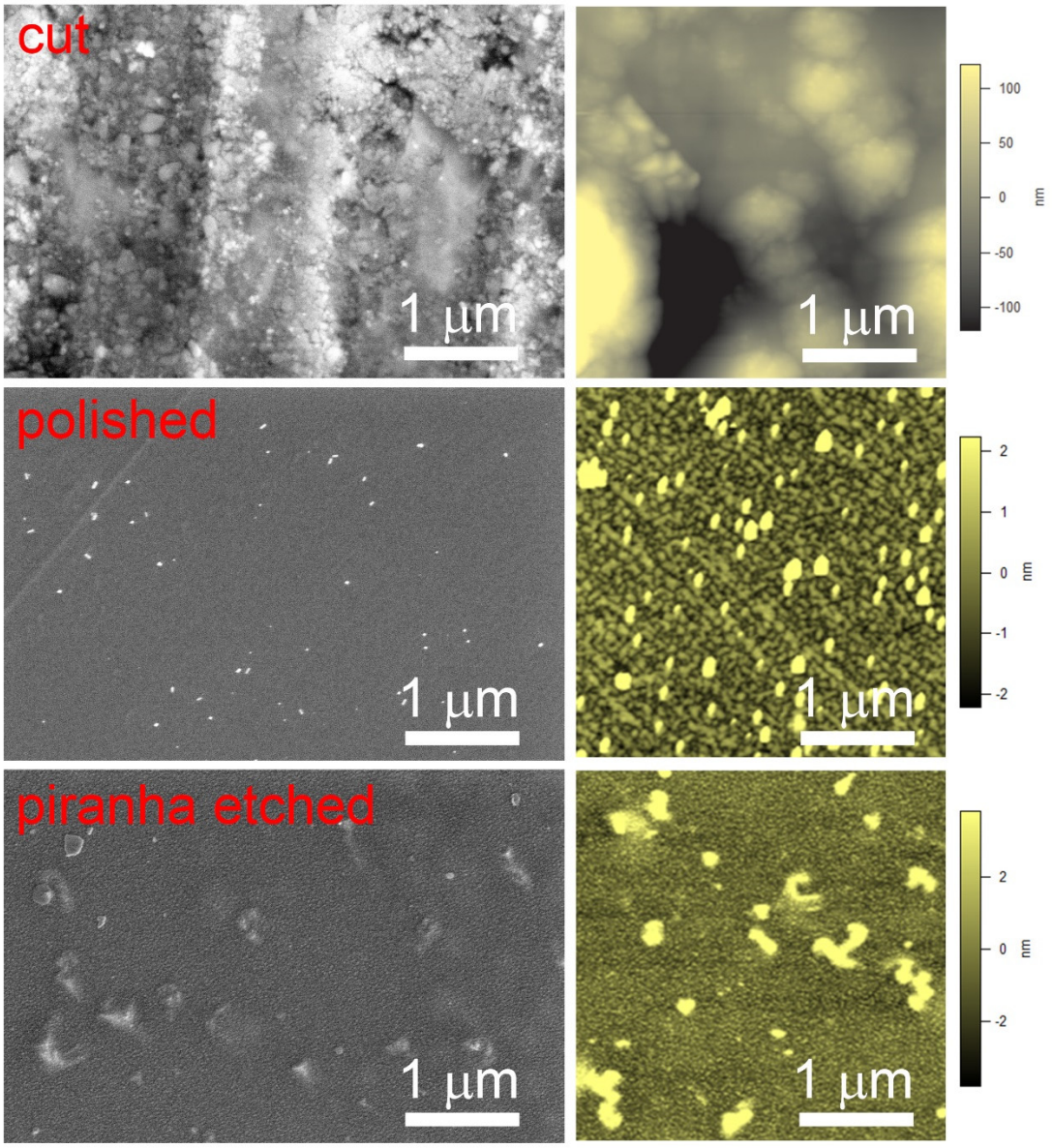

Figure S20. SEM and AFM images of the surface of a pyrite crystal (*top*) as cut with a diamond saw, (*middle*) after fine polishing, and (*bottom*) after etching the surface with piranha solution.

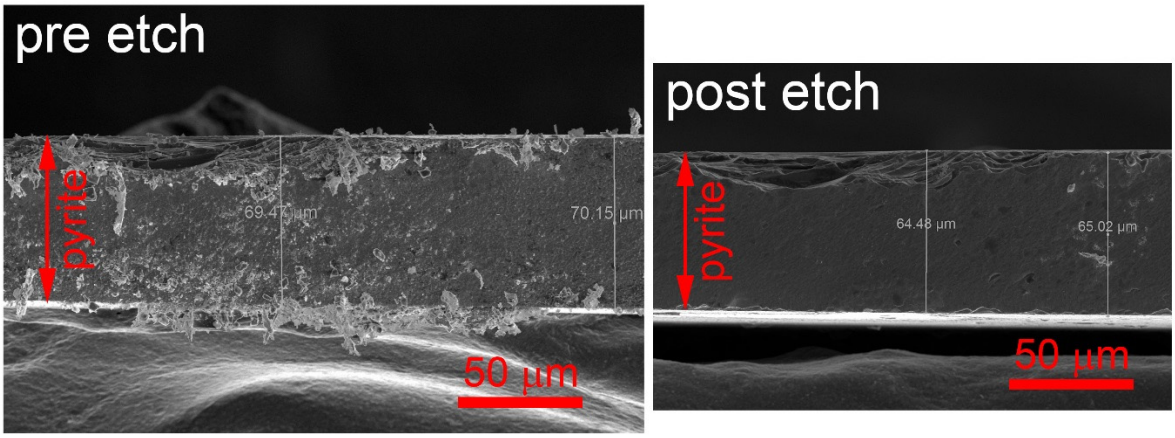

Figure S21. Cross-sectional SEM images of a pyrite crystal before and after a 5 min piranha etch. The etch rate is approximately 8 nm/s, assuming a constant activity of the piranha solution over 5 min.

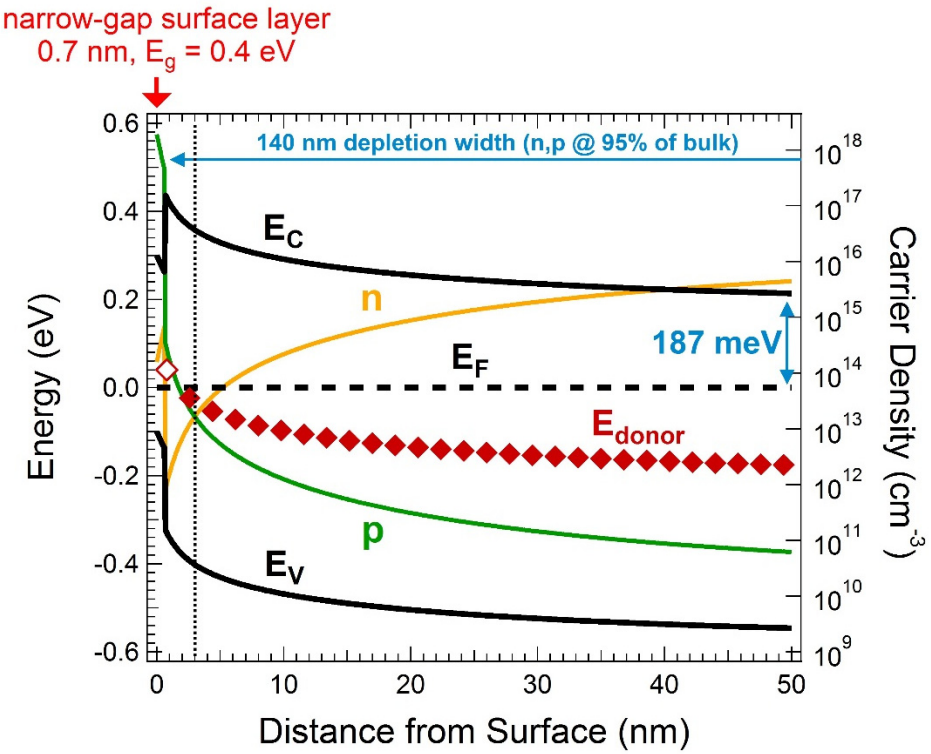

Figure S22. Calculated equilibrium band diagram of the pyrite surface at 300 K assuming the presence of a narrow-gap surface layer (E_g = 0.4 eV, 0.7 nm thick). In the bulk, E_F is located ~190 meV below the conduction band edge (consistent with $N_D = 6 \times 10^{19}$ cm^{-3} and $E_C - E_D$ = 390 meV from Hall data). At the surface, E_F is ~100 meV above the valence band edge (consistent with UPS data). Equilibration of bulk with surface results in relatively weak band bending of ~250 meV, which represents the upper limit for the pyrite V_{OC}. Thus, tunneling is unnecessary to explain the low V_{OC} if a narrow-gap surface layer is present. An inversion layer ($p > n$) approximately 3.0 nm thick is also created (denoted by the vertical dotted line). The inversion layer is separated from bulk by a depletion layer approximately 140 nm thick (defined here as $n = 0.95n_{bulk}$). The bulk pyrite band gap is assumed to be 0.76 eV.

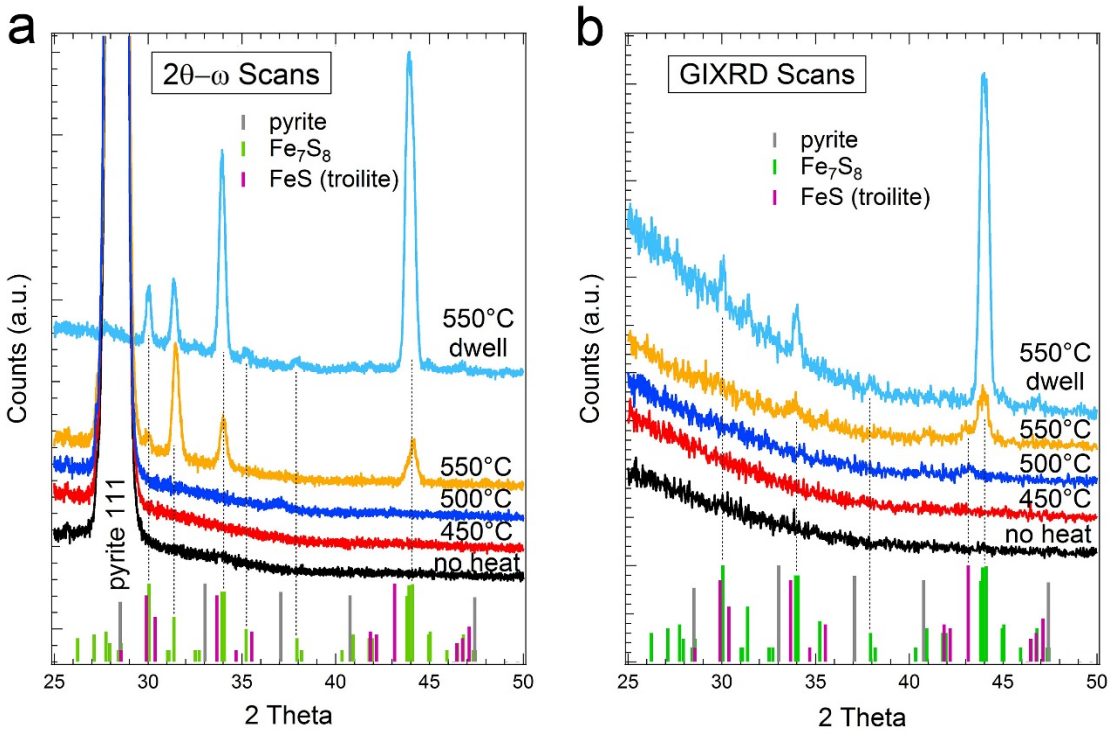

Figure S23. XRD patterns of a pyrite (111) single crystal before and after heating to progressively higher temperatures in ultrapure nitrogen. (a) 2θ-ω scans. (b) Omega scans with a grazing incidence angle of 1.0 degree. The sample was heated within 60 minutes to the temperature indicated, held at that temperature for 1 minute, and then cooled to room temperature within 60 minutes prior to data acquisition. The data labeled "550ºC dwell" were acquired after holding the sample at 550ºC for 1 hour.

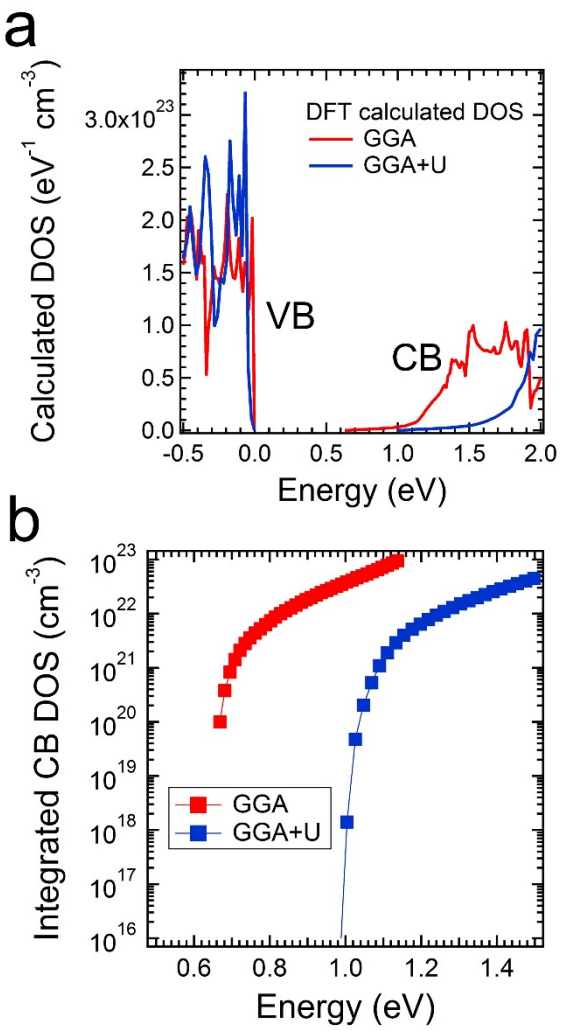

Figure S24. (a) The valence and conduction band density of states calculated by DFT using the GGA (red) and GGA+U (blue) levels of theory. (b) The integrated density of states for the conduction band at the two levels of theory. DFT results are taken from J. Hu, Y. Zhang, M. Law and R. Wu, *Phys. Rev. B*, 2012, **85**, 085203.

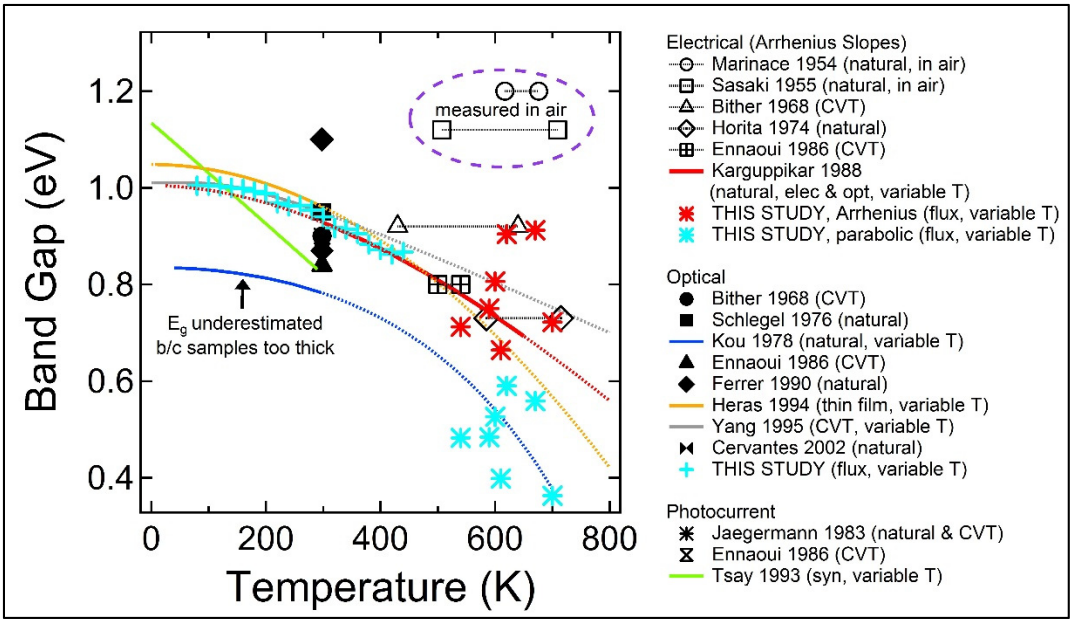

Figure S25. Compilation of literature values for the pyrite band gap. Dashed curves are extrapolations/interpolations from the variable-temperature experimental data (solid curves or points). The light blue crosses (optical data), light blue stars (electrical data modeled with the parabolic DOS(*E*)), and red stars (electrical data fit with simple Arrhenius lines) are the results of the present study.

References for Figure S25

Marinace 1954: J. C. Marinace, *Phys. Rev.* 1954, **96**, 593.

Sasaki 1955: A. Sasaki, *Minear. J.*, 1955, **1**, 290.

Bither 1968: T. A. Bither, R. J. Bouchard, W. H. Cloud, P. C. Donohue and W. J. Siemons, *Inorg. Chem.*, 1968, **7**, 2208.

Horita 1974: H. Horita and T. Suzuki, *Science reports of the Research Institutes, Tohoku University. Ser. A, Physics, chemistry and metallurgy*, 1974, **25**, 124.

Ennaoui 1986: A. Ennaoui and H. Tributsch, *J. Electroanal. Chem.*, 1986, **204**, 185.

Ennaoui 1986: A. Ennaoui, S. Fiechter, W. Jaegermann and H. Tributsch, *J. Electrochem. Soc.*, 1986, **133**, 97.

Karguppikar 1988: A. M. Karguppikar and A. G. Vedeshwar, *Phys. Stat. Sol. (a)*, 1988, **109**, 549.

Schlegel 1976: A. Schlegel and P. Wachter, *J. Phys. C*, 1976, **9**, 3363.

Kou 1978: W. W. Kou and M. S. Seehra, *Phys. Rev. B*, 1978, **18**, 7062.

Ferrer 1990: I. J. Ferrer, D. M. Nevskala, C. de las Heras and C. Sanchez, *Solid State Commun.* 1990, **74**, 913.

Jaegermann 1983: W. Jaegermann and H. Tributsch, *J. Appl. Electrochem.*, 1983, **13**, 743.

Heras 1994: C. de las Heras, I. J. Ferrer and C. Sanchez, *J. Phys.: Condens. Matter*, 1994, **6**, 10177.

Yang 1995: T.-R. Yang, J.-T. Yu, J.-K. Huang, S.-H. Chen, M.-Y. Tsay and Y.-S. Huang, *J. Appl. Phys.* 1995, **77**, 1710.

Cervantes 2002: P. Cervantes, Z. Slanic, F. Bridges, E. Knittle and Q. Williams, *J. Phys. Chem. Solids*, 2002, **63**, 1927.

Tsay 1993: M.-Y. Tsay, Y.-S. Huang and Y.-F. Chen, *J. Appl. Phys.* 1993, **74**, 2786.

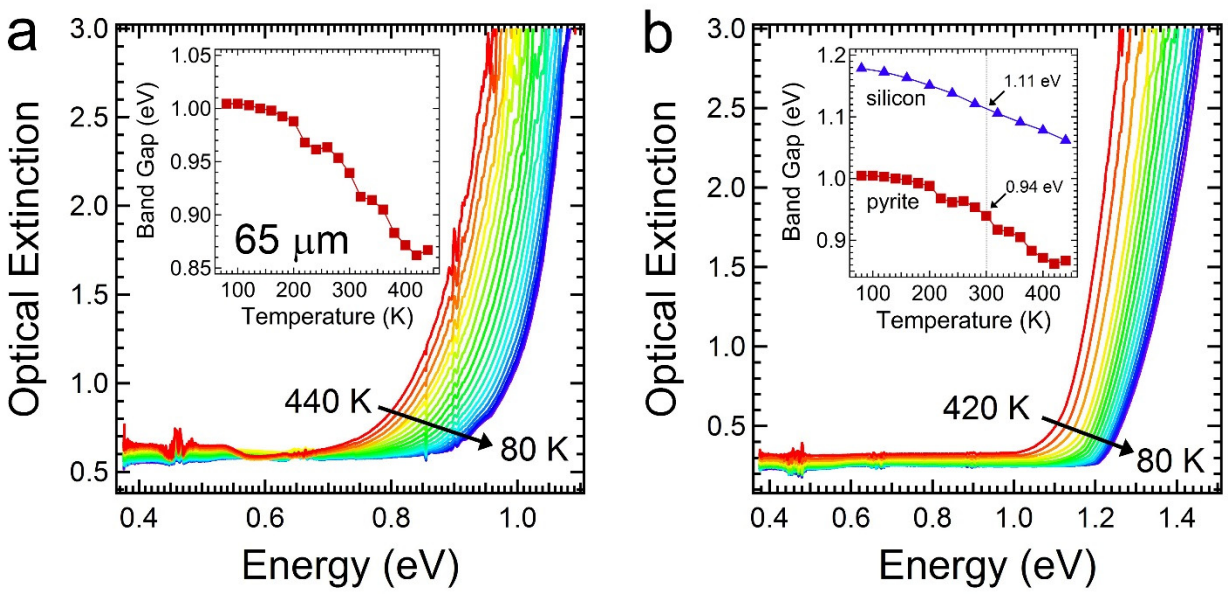

Figure S26. Optical extinction spectra of (a) a 65 μm thick pyrite crystal and (b) a 250 μm thick silicon crystal as a function of temperature. The crystals are polished on both sides. Data were acquired in 20 K increments. Inset are plots of band gap extracted from the raw extinction data after correcting for sample thickness and the dispersion of the refractive index. The inset in (b) compares the temperature dependence of the band gap for both materials. The room-temperature band gap of pyrite and silicon is 0.94 eV and 1.11 eV, respectively.

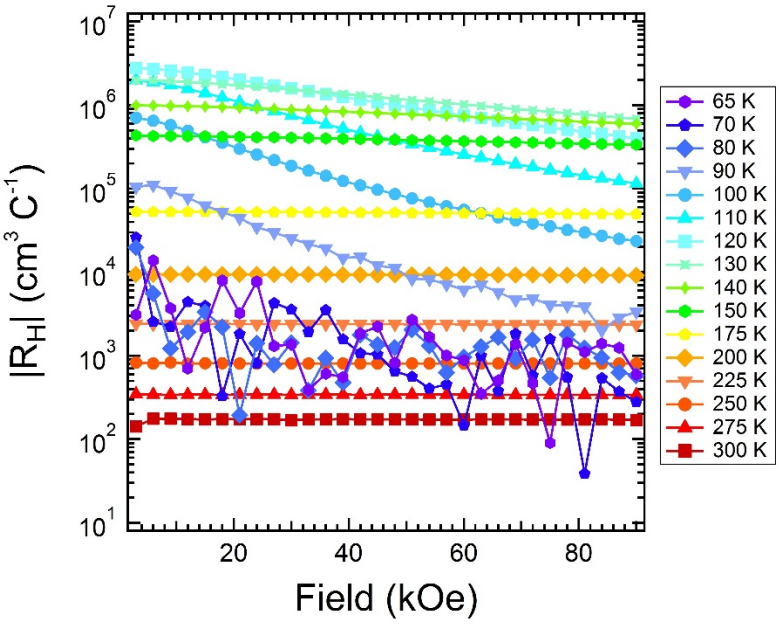

Figure S27. Representative plots of Hall coefficient versus magnetic field for a pyrite crystal as a function of temperature (65-300 K). In the unipolar region (T > 150 K), R_H is constant with field (in other words, the Hall voltage is linear with magnetic field). In the mixed-carrier region (intermediate temperatures), R_H decreases with increasing field. Finally, for T < 90 K, R_H becomes noisy but appears to flatten out with increasing field at higher values of applied field.

Derivation of logarithmic derivative expression used to linearize the equation $\boldsymbol{\rho(T) = \rho_0 \exp[(T_0/T)^p]}$:

$\rho = \rho_0 \exp[(T_0/T)^p]$

Take log: $\ln(\rho) = \ln(\rho_0) + (T_0/T)^p$

$$\frac{d(\ln \rho)}{d(\ln T)} = ?$$

Make substitution: $u = \ln(T) \rightarrow T = e^u$

Replace *T* with e^u: $\ln(\rho) = \ln(\rho_0) + (T_0/e^u)^p$

$$\ln(\rho) = \ln(\rho_0) + T_0^p e^{-pu}$$

Take derivative with respect to *u*: $\frac{d(\ln \rho)}{du} = -pT_0^p e^{-pu} = -p(T_0/e^u)^p$

Change back to T: $\frac{d(\ln \rho)}{d(\ln T)} = -p(T_0/T)^p$

Multiply by -1 and take log again: $\ln\left(-\frac{d(\ln \rho)}{d(\ln T)}\right) = \ln(p) + \ln(T_0/\mathrm{T})^p$

$$\ln\left(-\frac{d(\ln \rho)}{d(\ln T)}\right) = \ln(p) + p\ln(T_0) - p\ln(T) = \text{constant} - p\ln(T)$$